PIER C

Systematic Synthesis of Fully-Planar Antennas Based on Metamaterial-Enhanced SIWs for 5G Communications

Vasileios Salonikios[1], Stamatios Amanatiadis[1], and Michalis Nitas[2,*]

[1]*Department of Electrical and Computer Engineering, Aristotle University of Thessaloniki, Greece*
[2]*Department of Space Research and Technology, Technical University of Denmark, Bld. 348,*
Ørsteds Plads, 2800 Kgs. Lyngby, Denmark

ABSTRACT: A fully numerical process for the systematic design of fully-planar antennas for 5G communications frequencies is presented, utilizing a metamaterial-enhanced SIW as the basis platform. A combined modal analysis and wave propagation Finite Element modeling is proposed for the accurate design of the waveguiding structure towards its leakage loss minimization. Based on this robust numerical scheme, two different types of fully-planar antennas are designed. A leaky-wave fully-planar two-slot antenna and an H-plane end-fire sectoral horn antenna. Both structures are viable candidates for integration in 5G communications platforms, exhibiting attractive characteristics such as optimized gain and bandwidth, low cost, compactness, and ease of fabrication.

1. INTRODUCTION

The recent emergence of 5G communications has urged the need for the utilization of higher frequency spectrum, with a consequent demand for the design of new components, capable of being integrated at the same substrate. Indeed, the rising requirements for higher data bit-rates have caused the transition of the microwave and mm-wave structures to smaller dimensions, to enable their operation in modern circuits. Substrate Integrated Waveguide (SIW) constitutes the established transmission line which has been utilized in a variety of microwave circuits, for the efficient and low-loss transmission of the electromagnetic wave [1, 2]. Additionally, a plethora of other SIW-based components have also been designed and integrated in various platforms, such as antennas, couplers, dividers, and cavities, in this way realizing the required structures for the establishment of 5G communication channels [3–9].

Recently, an alternative SIW type was proposed, metamaterial-inspired SIW [10]. This novel transmission line utilizes complementary split-ring resonators (CSRRs), which substitute the vias of a classical SIW and provide a visual electric wall for the efficient channeling of the electromagnetic wave. The main advantages of the CSRR-SIW are the accomplishment of lower leakage losses and the avoidance of holes drilling, rendering the structure fully planar and capable of being totally fabricated through a classical development and etching chemical process. Its utilization as a waveguiding basis for other components has led to the design of multiple structures, such as leaky-wave antennas and power couplers [11, 12]. Furthermore, interesting alternatives of the utilized metamaterial resonators have been proposed recently, along with studies on the sensitivity of the resonators' misalignment [13, 14].

We present a systematic process for the efficient, accurate synthesis of compact fully-planar antennas, based on the concept of the metamaterial-enhanced SIW. Initially, in Section 2, we propose a rigorous, fully-numerical procedure for the optimal design of a CSRR-SIW for 5G communication frequencies, the basis structure on which the antennas are built on: We make use of the combined eigenvalue periodic structure analysis and the novel excitation FEM schemes, both based on the alternative field-flux FEM formulations [15–18]. In this way, the optimal dimensions of the waveguiding structure are guaranteed, in terms of the minimization of the leakage losses at specified frequency zones. Subsequently, we design, optimize, simulate, and measure two different types of antennas: A two-slot fully-planar antenna in Section 3 and an end-fire sectoral horn antenna in Section 4. Both structures are designed so as to work around 27 GHz, optimized with respect to maximum bandwidth and gain.

2. DESIGN OF THE FULLY PLANAR CSRR-SIW

The first step for the synthesis of the CSRR-SIW-based antennas is the determination of the waveguiding characteristics of a CSRR-SIW. To this end, we initially perform an eigenvalue analysis of the unit cell of the waveguide [Fig. 1(a)], in order to extract the characteristics of its guided mode, i.e., the field distribution, the complex propagation constant, and the wave impedance. The optimal dimensions of the utilized resonators have been derived using formerly proposed parameter retrieval techniques [19–21]. Subsequently, we describe the wave propagation (excitation) study, which utilizes the eigenvalue analysis results to efficiently excite the waveguiding structure.

---

* Corresponding author: Michalis Nitas (mnitas@auth.gr).
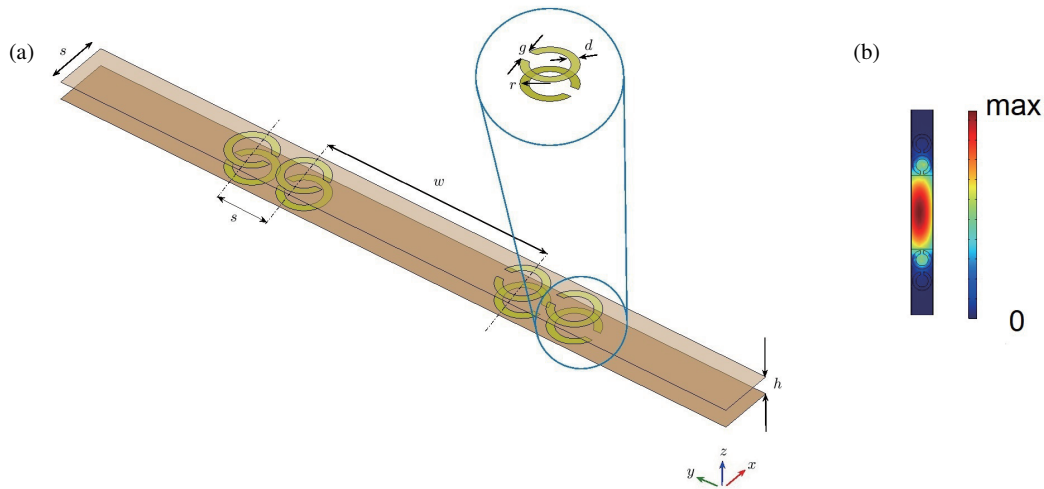
FIGURE 1. (a) The SRR-SIW unit cell: effective width (w), ring spacing (s), ring gap (g), ring external radius (r), ring width (d) and PCB width (h). The propagation axis is the x axis. (b) Field distribution of the electric field norm at the middle of the dielectric substrate at 27 GHz.

2.1. Numerical Tools I: Eigenmode Analysis

We utilize the field-flux **e-b** eigenmode finite element method (FEM) formulation to perform a spurious-free eigenmode analysis of the waveguide's unit cell [Fig. 1(a)] in order to obtain the propagation constant β (rad/m) and the attenuation constant α (Np/m) of the supported eigenmode, along with the corresponding field distribution [15, 17]. Very briefly, according to the Bloch-Floquet theorem, we may write the electric field intensity **E** and the magnetic flux density **B** as a product of their periodic envelopes **e** and **b**, respectively, and an exponential factor $e^{-j\mathbf{k}\cdot\mathbf{r}}$ as

$$\mathbf{E} = \mathbf{e}e^{-j\mathbf{k}\cdot\mathbf{r}} \tag{1a}$$

$$\mathbf{B} = \mathbf{b}e^{-j\mathbf{k}\cdot\mathbf{r}}, \tag{1b}$$

where $\mathbf{k} = k\hat{\mathbf{k}}$ is the Bloch-Floquet wavevector of prescribed propagation direction $\hat{\mathbf{k}}$ (e.g., $\hat{\mathbf{k}} = \hat{\mathbf{x}}$), and $k = \beta - j\alpha$ is the unknown complex propagation constant. Under the aforementioned transformations, the Maxwell's curl equations may be rewritten as follows:

$$\nabla \times \mathbf{e} - jk\hat{\mathbf{k}} \times \mathbf{e} = -j\omega\mathbf{b} \tag{2a}$$

$$\nabla \times \bar{\bar{\mu}}_{\mathrm{r}}^{-1}\mathbf{b} - jk\hat{\mathbf{k}} \times \bar{\bar{\mu}}_{\mathrm{r}}^{-1}\mathbf{b} = j\omega\epsilon_0\mu_0\bar{\bar{\epsilon}}_{\mathrm{r}}\mathbf{e}, \tag{2b}$$

where ω is the angular frequency, and $\bar{\bar{\epsilon}}_{\mathrm{r}}$ and $\bar{\bar{\mu}}_{\mathrm{r}}$ are the 3×3 tensors of relative dielectric permittivity and relative magnetic permeability, respectively. Using test functions $\mathbf{e}'$ and $\mathbf{b}'$ to weight Eqs. (2a) and (2b), respectively, and integrating over the volume of a unit cell, we obtain the Galerkin formulation of the problem

$$\iiint_V \mathbf{b}' \cdot \nabla \times \mathbf{e}\, \mathrm{d}V - jk \iiint_V \mathbf{b}' \cdot \hat{\mathbf{k}} \times \mathbf{e}\, \mathrm{d}V$$

$$= -j\omega \iiint_V \mathbf{b}' \cdot \mathbf{b}\, \mathrm{d}V \tag{3a}$$

$$\iiint_V \bar{\bar{\mu}}_{\mathrm{r}}^{-1}\mathbf{b} \cdot \nabla \times \mathbf{e}'\, \mathrm{d}V - jk \iiint_V \mathbf{e}' \cdot \hat{\mathbf{k}} \times \bar{\bar{\mu}}_{\mathrm{r}}^{-1}\mathbf{b}\, \mathrm{d}V$$

$$= j\omega\epsilon_0\mu_0 \iiint_V \mathbf{e}' \cdot \bar{\bar{\epsilon}}_{\mathrm{r}}\mathbf{e}\, \mathrm{d}V + \oiint_S (\mathbf{e}' \times \bar{\bar{\mu}}_{\mathrm{r}}^{-1}\mathbf{b}) \cdot \hat{\mathbf{n}}\, \mathrm{d}S, \tag{3b}$$

where $\hat{\mathbf{n}}$ denotes the unitary vector normal to the boundary, pointing outward from the boundary surfaces, V the total volume of the unit cell, and S the enclosing surface. The discretization of Eqs. (3a) and (3b) is done by using the appropriate vector element expansion functions and results in the following matrix form

$$\begin{bmatrix} -j\omega\epsilon_0\mu_0\mathbf{T}^{E'E} + \mathbf{T}_s^{E'E} & \mathbf{Q}^{E'B} - \mathbf{T}_s^{E'B} \\ \mathbf{Q}^{B'E} & j\omega\mathbf{T}^{B'B} \end{bmatrix} \begin{bmatrix} \mathbf{E} \\ \mathbf{B} \end{bmatrix} =$$

$$k \begin{bmatrix} 0 & -j\mathbf{P}^{E'B} \\ -j\mathbf{P}^{B'E} & 0 \end{bmatrix} \begin{bmatrix} \mathbf{E} \\ \mathbf{B} \end{bmatrix}, \tag{4}$$

where the submatrices are defined in [15]. Eq. (4) is an eigenvalue problem where angular frequency ω is a parameter; the wavenumber k is the eigenvalue; and the corresponding eigenvector is the field distribution of the periodic envelopes **e** and **b**.

2.2. Numerical Tools II: Wave Propagation Study

Following the acquisition of the waveguiding characteristics of the SIW through its eigenmode computation, we move on to the excitation of a waveguiding structure consisting of multiple unit cells. The wave propagation (excitation) problem for the waveguide is solved by utilizing the **E-B** FEM excitation formulation. The most general case of this formulation, including arbitrarily bianisotropic materials is examined in [17]. Here, we present the FEM formulation for the excitation case of an SIW. After scaling the magnetic induction field **B** by multiplying it with the speed of light in vacuum c_0, we write the Maxwell's equations in frequency domain (assuming a $e^{+j\omega t}$ time dependence)

$$\nabla \times \mathbf{E} + k_0\tilde{\mathbf{B}} = 0 \tag{5a}$$

TABLE 1. Optimal dimensions of the proposed CSRR-SIW.

Central frequency (GHz)	Outer radius r (mm)	Ring width d (mm)	Ring gap g (mm)	SIW width w (mm)	Substrate height h (mm)	Unit cell s (mm)
27	0.84	0.3	0.3	6.5	0.8001	1.88

$$\nabla \times \bar{\bar{\mu}}_r^{-1} \tilde{\mathbf{B}} + k_0 \bar{\bar{\epsilon}}_r \mathbf{E} = 0. \tag{5b}$$

The Galerkin formulation for Eqs. (5a) and (5b) is derived by weighting the first equation with test function $\mathbf{B}'$ and the second one with test function $\mathbf{E}'$, and integrating over the volume V of the computational domain. The final weak formulation yields

$$\iiint_V \mathbf{B}' \cdot \nabla \times \mathbf{E} \, dV + k_0 \iiint_V \mathbf{B}' \cdot \tilde{\mathbf{B}} \, dV = 0 \tag{6a}$$

$$\iiint_V \nabla \times \mathbf{E}' \cdot \bar{\bar{\mu}}_r^{-1} \tilde{\mathbf{B}} \, dV + k_0 \iiint_V \mathbf{E}' \cdot \bar{\bar{\epsilon}}_r \mathbf{E} \, dV$$
$$= - \oiint_S \mathbf{E}' \cdot \hat{\mathbf{n}} \times \bar{\bar{\mu}}_r^{-1} \tilde{\mathbf{B}} \, dS. \tag{6b}$$

Approximating this weak formulation by the same basis functions, utilized in the previous section, we derive the following matrix equation

$$\begin{bmatrix} k_0 \mathbf{T}^{E'E} & \mathbf{Q}^{E'B} \\ \mathbf{Q}^{B'E} & k_0 T^{B'B} \end{bmatrix} \begin{bmatrix} \mathbf{E} \\ \tilde{\mathbf{B}} \end{bmatrix} = \begin{bmatrix} T_s^{E'E} & T_s^{E'B} \\ T_s^{B'E} & T_s^{B'B} \end{bmatrix} \begin{bmatrix} \mathbf{E} \\ \tilde{\mathbf{B}} \end{bmatrix}, \tag{7}$$

with the corresponding matrices calculated in [17].

We now derive the proper boundary condition which efficiently excites and absorbs the provided mode in a structure. The transverse electric and magnetic components of an electromagnetic field propagating in $\hat{\mathbf{k}}$ direction fulfill the equation

$$\mathbf{H}_t = \bar{\bar{Z}}_w^{-1} \hat{\mathbf{k}} \times \mathbf{E}, \tag{8}$$

where index t denotes the transverse part of the field, and Z_w is the dyadic wave impedance. We take the cross product of Eq.? (8) with the unit vector $\hat{\mathbf{n}}$ pointing outward form the port boundary surface as

$$\hat{\mathbf{n}} \times \mathbf{H} = \hat{\mathbf{n}} \times \mu_0^{-1} \bar{\bar{\mu}}_r^{-1} \mathbf{B} = \hat{\mathbf{n}} \times \bar{\bar{Z}}_w^{-1} \hat{\mathbf{k}} \times \mathbf{E}. \tag{9}$$

Taking the scaling factor into account, this yields

$$\hat{\mathbf{n}} \times \bar{\bar{\mu}}_r^{-1} \tilde{\mathbf{B}} = jc_0 \mu_0 \hat{\mathbf{n}} \times \bar{\bar{Z}}_w^{-1} \hat{\mathbf{k}} \times \mathbf{E}. \tag{10}$$

The electric field fulfills the condition $\mathbf{E} = \mathbf{E}_{inc} + \mathbf{E}_{ref}$ at the input port, for the incident ($\hat{\mathbf{k}} = -\hat{\mathbf{n}}$) and reflected field ($\hat{\mathbf{k}} = \hat{\mathbf{n}}$), therefore Eq. (10) becomes

$$\hat{\mathbf{n}} \times \bar{\bar{\mu}}_r^{-1} \tilde{\mathbf{B}} = -2jc_0 \mu_0 \hat{\mathbf{n}} \times \bar{\bar{Z}}_w^{-1} \hat{\mathbf{n}} \times \mathbf{E}_{inc} + jc_0 \mu_0 \hat{\mathbf{n}} \times \bar{\bar{Z}}_w^{-1} \hat{\mathbf{n}} \times \mathbf{E}. \tag{11}$$

The corresponding output Absorbing Boundary Condition (ABC) port, capable of solely absorbing a propagating mode is given by Eq. (11) setting $\mathbf{E}_{inc} = 0$. The final surface integral expressions which need to be calculated at the input port

boundary are derived by inserting Eq. (11) in the the right hand side of Eq. (6b) of the derived Galerkin formulation, which gives

$$- \oiint_S \mathbf{E}' \cdot \hat{\mathbf{n}} \times \bar{\bar{\mu}}_r^{-1} \tilde{\mathbf{B}} \, dS =$$

$$-2jc_0 \mu_0 \oiint_S \mathbf{E}' \cdot \hat{\mathbf{n}} \times \bar{\bar{Z}}_w^{-1} \hat{\mathbf{n}} \times \mathbf{E}_{inc} \, dS$$

$$+jc_0 \mu_0 \oiint_S \mathbf{E}' \cdot \hat{\mathbf{n}} \times \bar{\bar{Z}}_w^{-1} \hat{\mathbf{n}} \times \mathbf{E} \, dS. \tag{12}$$
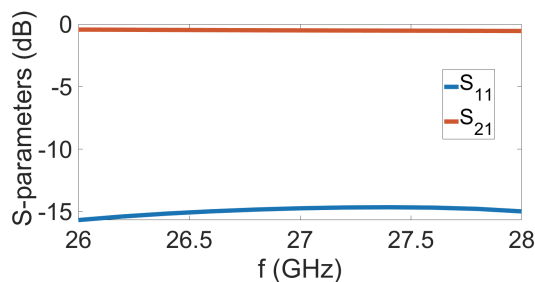
2.3. Optimized Configuration for 5G Communications Frequencies

Here, we present the optimal configuration of the CSRR-SIW in terms of minimization of its attenuation constant α, resulting from the combined numerical treatment of the previous two subsections. The optimal dimensions for a frequency zone of 26–28 GHz are given in Table 1, derived by a parametric analysis which includes all the geometric parameters of the CSRR-SIW unit cell shown in Fig. 1(a). In Fig. 1(b), we illustrate the field distribution of the supported mode of the optimal SRR-SIW, resulting from the solution of Eq. (4). In the simulations, a Taconic substrate was utilized, with a relative dielectric constant of $\epsilon_r = 2.2$, $\tan \delta = 0.001$ and a thickness of 0.8001 mm. For conductor losses, the metal parts are modeled by the proper Impedance Boundary Condition (IBC) [15] assuming a thickness of 17 μm and a typical copper conductivity σ of $5.88 \cdot 10^7$ S/m.

The complex propagation constant with respect to frequency for the optimal configuration is illustrated in Fig. 2, whereas the diagram of the wave impedance Z_w is given in Fig. 3. In Fig. 4, the transmission and reflection of the waveguide throughout the simulated frequency zone are depicted in terms of its S-parameters. For their extraction, the solution of Eq. (7) was utilized, where the involved quantities E_{inc} and Z_w were taken from the corresponding solutions of the eigenvalue problem at every simulated frequency. The structure's potential to efficiently guide the electromagnetic wave at frequencies between 26 and 28 GHz is guaranteed. Performance comparison of the optimal waveguiding structure with the existing designs in the literature, including the classical SIW designs, is thoroughly presented in [10], where the superiority of our proposed design is proved.
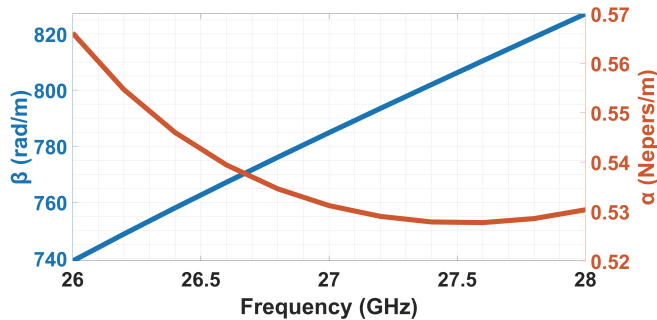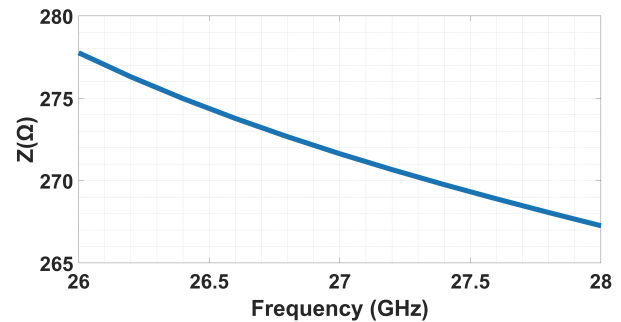
FIGURE 2. Diagrams of the propagation constant β (rad/m) and the attenuation constant α (Np/m) versus frequency for the optimal configuration of the CSRR-SIW at the simulated frequency zone of $26 - 28$ GHz.
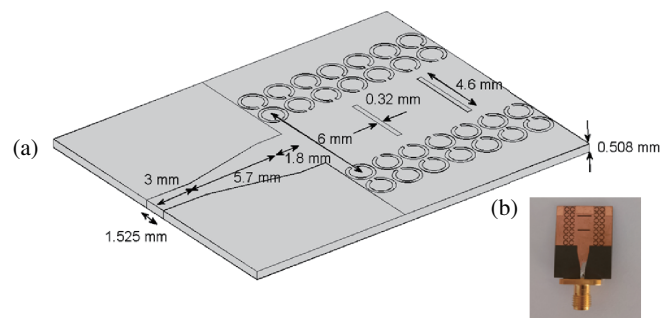

FIGURE 3. Plot of the wave impedance with respect to frequency for the optimal CSRR-SIW.

FIGURE 4. Return loss (S_{11}) and transmission coefficient (S_{21}) for the CSRR-SIW.

FIGURE 5. (a) The proposed two-slot CSRR-SIW-based antenna with its optimal dimensions. (b) The fabricated prototype.

3. TWO-SLOT COST-EFFECTIVE EASY-TO-FABRICATE FULLY-PLANAR ANTENNA OF OPTIMIZED GAIN

The successful design of the CSRR-SIW opens the way for the efficient synthesis of fully-planar slot antennas for operation at frequency bands for 5G communications. Considering that there is a wide and diverse variety of possible 5G wireless applications, these antennas should be based on a design that is flexible and scalable and that retains the fully-planar and low-profile geometry of the CSRR-SIW. A suitable solution to this problem is the class of leaky-wave antennas, where the radiation leakage is obtained by the proper opening of a series of transverse slots on the upper boundary of the waveguide [22–30]. Drawing our inspiration from the design of the slotted array antennas, a simple design of a CSRR-SIW antenna consists of two resonant slots with a distance of $\lambda_g/2$ (λ_g is the guided wavelength), as shown in Fig. 5. The efficient channeling of the electromagnetic energy in the waveguide depends heavily on the polarization and the angle of incidence of the wave, and thus, fine tuning of both the slot dimensions and the distance between the slots is required. The antenna is terminated at a short-circuited printed circuit board (PCB), in this way utilizing the standing wave propagation mechanism. Furthermore, a matching circuit consisting of a tapered microstrip line is properly designed, in order to match the 50-Ohm impedance of the feeding coaxial cable. The antenna was designed on an RT/Duroid laminate of height $h = 0.508$ mm with a complex relative dielectric constant $\epsilon_r = 2.2 - j0.0009$. In the simulations, the antenna was

excited following the procedure described in Section 2. The structure was optimized towards its bandwidth enhancement at a central frequency of 27 GHz, through a parametric analysis, where the geometric parameters of the slot lengths, slots' position, and the distance of the second slot from the short-circuited end were utilized.

The antenna's return loss in terms of its S_{11} parameter is illustrated in Fig. 6. A very good agreement between the simulated and measured results is observed, with a measured central operation frequency of 26.9 GHz and a bandwidth of approximately 1.7 GHz. The simulated 3D far field radiation pattern at 27 GHz is illustrated in Fig. 7. A broadside radiation behavior is exhibited, with a maximum of approximately 9 dBi normal to its plane. The measured far field radiation pattern at 27 GHz at a yz-plane is depicted in Fig. 8. It is observed that the measure-
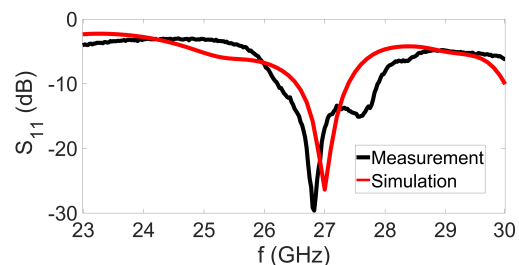
FIGURE 6. Simulated and measured return losses for the two-slot antenna.
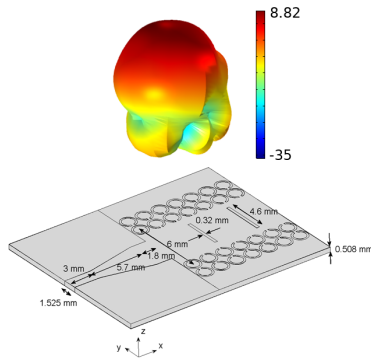
FIGURE 7. Simulated 3D-radiation pattern of the two-slot antenna at 27 GHz. The antenna exhibits a maximum gain of approximately 9 dBi.
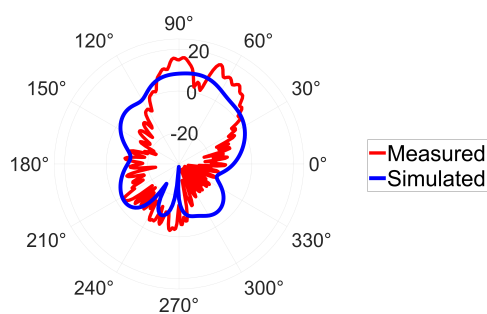
FIGURE 8. Measured and simulated far fields of the two-slot antenna at 27 GHz at H-plane.

ment confirms the broadside radiation of the antenna. A dip is visible at an angle of about 15 degrees from the normal, which may be attributed to the following two main factors: First, due to fabrication errors, it is almost sure that the exact position and the dimensions of the slots deviate from those in the simulation; therefore, the measured far field is modified from the desired (simulated) case. Second, the excitation of the antenna in the simulation was conducted in the ideal way described in Section 2, i.e., it was the supported eigenmode of the SIW that excited the structure, whereas in the fabricated sample, we make use of a coaxial SMA connector, that produces a discontinuity between the feeding cable and the structure. Therefore, it is certain that this discontinuity disturbs the mode inserted inside the antenna, in this way affecting the antenna's far field. In Table 2, we depict the comparison of our proposed antenna with a similar two-slot SIW-antenna design in [23], in terms of the operational bandwidth and maximum gain at the central frequency of each proposed antenna. There is an obvious superiority of our design, both at the operational bandwidth and at the maximum achieved gain.

**TABLE 2**. Comparison with similar slot antenna.

|	Freq. [GHz]	BW [GHz]	Max. Gain [dBi]
Ref. [23]	28	0.983	7.05
This work	26.9	1.7	9

4. H-PLANE END-FIRE SECTORAL HORN ANTENNA

The CSRR-SIW platform is also capable of supporting antenna designs featuring end-fire radiation. A characteristic example is the H-plane sectoral horn [31–39]. Here, the designed antenna is realized by flaring the CSRR structures of the waveguide, which forms the lateral sections of the horn. However, this substrate-integrated configuration does not allow for a gradual transition on the vertical plane, which, in turn, has a detrimental effect on the matching between the antenna and the air. This mismatch behavior intensifies for thin-substrate antennas, where the thickness of the substrate is lesser than $\lambda_0/10$, resulting in high reflection coefficients and unwanted radiation. This drawback, combined with the requirement of thin substrates for the proper operation of the CSRR-SIW platform, makes the design of such an antenna very challenging. A solution to overcome these difficulties is composed of a printed addition of a number of parallel plate matching strips, etched directly after the printed horn, as illustrated in Fig. 9. This addition retains the planar nature of the overall design and functions as a network of resonators improving the air-horn matching. The operation of this transition can also be considered as that of an array of parallel plate resonators irradiating from their individual apertures and fed through the aperture of the horn.

The crucial parameters for the design of the printed transition are its geometric characteristics that modify the array factor of the parallel plate array. The length of each parallel plate element, assuming that we have selected uniform dimensions for all elements and that the separation between every two elements is much smaller than the parallel plate length, controls the phase shift in the radiated power of two neighbouring elements, and the separation length between the elements determines the amount of power deposited in each parallel plate resonator. Larger separation gaps minimize the contribution of the subsequent element, while smaller separation gaps minimize the radiation output of the preceding element. This implies that there exists a separation gap, for which the amount of power deposited in each element is equal, and as a result, the radiation pattern of the array depends solely on the selection of the parallel plate element length.

This allows us to modify the radiation pattern of the antenna and enhance the Front-to-Back Ratio, by minimizing the back-end radiation with an appropriate selection of the parallel plate length. We have to point out that the backwards radiation can only be minimized and not cancelled, since the radiation losses in each element prevent the power deposits being equal in every parallel plate element even in the case of an optimally selected separation. The design parameters that were determined in order to increase the front-end gain and Front-to-Back Ratio and improve the matching behaviour are listed in Table 3. The antenna was analyzed using the Finite Element solvers of Comsol Multiphysics™ for the 5G frequency band of 26 to 28 GHz, utilizing the excitation procedure described in Section 2. The dielectric losses of the substrate and the conductive losses of the copper plates were taken into account (Taconic substrate of thickness 0.8001 mm, $\epsilon_r = 2.2$, $\tan \delta = 0.001$, conductivity $\sigma = 5.8 \cdot 10^7$ S/m). The simulations were conducted for approximately 3 million degrees of freedom (dofs).
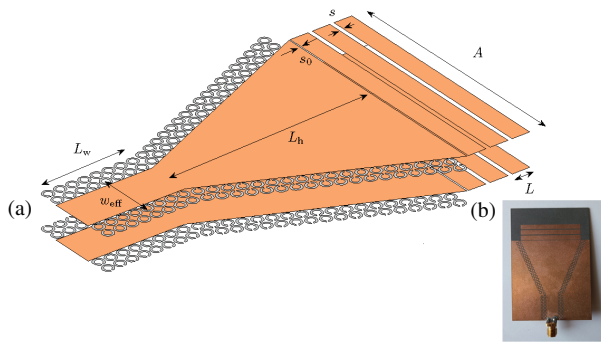
FIGURE 9. The BC-CSRR Horn antenna with a printed transition of parallel plate elements. (a) Geometric dimensions and (b) Fabricated sample.
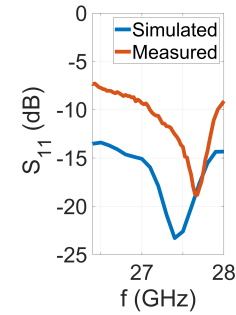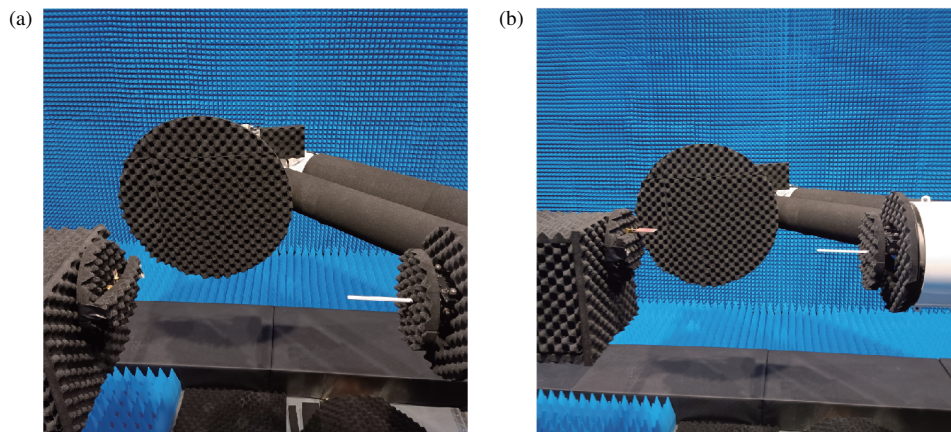

FIGURE 10. Simulated and measured return losses for the BC-CSRR Horn antenna.
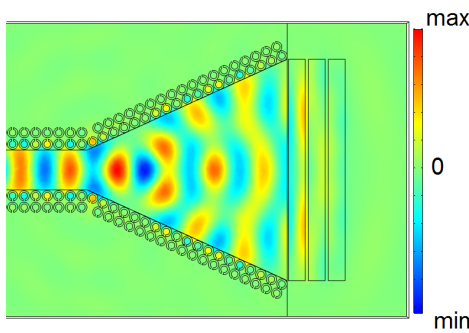
FIGURE 11. The z-component of the electric field distribution at the middle of the substrate at 27 GHz. The horn acts as a transition for the feed of the array of parallel plate elements. The axial length of the horn suffices for a minimized quadratic phase error.
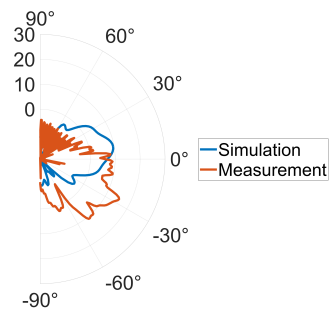
FIGURE 12. Simulated and measured radiation patterns for the horn antenna at 27 GHz.

FIGURE 13. Measurement setup for (a) the two-slot antenna of Section 3 and (b) the H-plane horn antenna of Section 4.

The measured and simulated return losses of the antenna are illustrated in Fig. 10, where its operation is easily observed in the designed frequency zone. In Fig. 11, the electric field distribution at the middle of the substrate is shown, whereas the simulated and measured far fields of the antenna at 27 GHz are depicted in Fig. 12, exhibiting an end-fire radiation behavior. The discrepancies between the simulated and measured values of the far field and S_{11} parameters may be attributed in this case

to the limits in fabrication precision and the finite accuracy of the FEM simulations. Indeed, the perfect matching between the antenna and the air that is achieved in the simulations, which were conducted in a very dense FEM mesh, cannot be guaranteed in the real, fabricated sample; therefore, this weakness is interpreted in the radiation pattern of the antenna and the tilt in its radiation diagram.

TABLE 3. Optimized dimensions of the proposed sectoral horn antenna.

Symbol	Quantity	Dimensions (mm)
L_h	Horn Length	32.5
A	Horn Aperture Width	36
s_0	Horn Printed Transition Gap	0.2
s	Transition Element Separation Gap	0.5
L	Parallel Plate Strip Length	2.75
N_e	Number of Elements	3
W_{eff}	BC-CSRR SIW width	6.5
L_w	BC-CSRR SIW Length	15

In Table 4, we depict the comparison of our proposed antenna with similar designs in the literature [33, 40–43], in terms of the size and their maximum gain at the central frequency of operation. Our design achieves one of the highest gains among the compared structures, with its overall size being of average dimensions. We finally note that the proposed antennas in this work were measured at the DTU-ETC mm-Wave Antenna Test Facility. The measurement setup is provided in Fig. 13.

TABLE 4. Comparison with similar H-plane antenna designs.

	Freq. [GHz]	Size [$\lambda \times \lambda \times \lambda$]	Max. Gain [dBi]
Ref. [33]	28	$2.24 \times 0.14 \times 2.78$	5.5
Ref. [40]	30	$2.61 \times 0.17 \times 3.46$	10
Ref. [41]	16.6	$1.80 \times 0.08 \times 3.26$	5.5
Ref. [42]	35.5	$1.89 \times 0.18 \times 3.47$	9.3
Ref. [43]	35	$2.30 \times 0.17 \times 4.40$	6.8
This work	27.5	$2.92 \times 0.72 \times 3.24$	10

5. CONCLUSION

This work constitutes a complete study on the systematic synthesis of fully-planar antennas based on substrate-integrated waveguides. We initially describe the computational frame, which utilizes the robust finite element field-flux schemes for the accurate design of the metamaterial-based SIW, a rigorous process that guarantees the optimized wave propagation, with minimized attenuation constant. Based on this waveguide, we subsequently design, optimize, and measure two different types of antennas: A two-slot easy-to-fabricate leaky-wave antenna of optimized gain and an H-plane end-fire horn antenna, both capable of operating at the 27 GHz 5G frequency zones.

ACKNOWLEDGEMENT

REFERENCES

[1] Nwajana, A. O. and E. R. Obi, "A review on SIW and its applications to microwave components," *Electronics*, Vol. 11, No. 7, 1160, 2022.

[2] Bozzi, M., A. Georgiadis, and K. Wu, "Review of substrate-integrated waveguide circuits and antennas," *IET Microwaves, Antennas & Propagation*, Vol. 5, No. 8, 909–920, 2011.

[3] Milias, C., R. B. Andersen, P. I. Lazaridis, Z. D. Zaharis, B. Muhammad, J. T. B. Kristensen, A. Mihovska, and D. D. S. Hermansen, "Metamaterial-inspired antennas: A review of the state of the art and future design challenges," *IEEE Access*, Vol. 9, 89 846–89 865, 2021.

[4] Kumar, L., V. Nath, and B. V. R. Reddy, "A wideband substrate integrated waveguide (SIW) antenna using shorted vias for 5G communications," *AEU — International Journal of Electronics and Communications*, Vol. 171, 154879, 2023.

[5] Naseri, H., P. PourMohammadi, A. Iqbal, A. A. Kishk, and T. A. Denidni, "SIW-based self-quadruplexing antenna for microwave and mm-wave frequencies," *IEEE Antennas and Wireless Propagation Letters*, Vol. 21, No. 7, 1482–1486, 2022.

[6] Serhsouh, I., M. Himdi, H. Lebbar, and H. Vettikalladi, "Reconfigurable SIW antenna for fixed frequency beam scanning and 5G applications," *IEEE Access*, Vol. 8, 60 084–60 089, 2020.

[7] Lu, R., C. Yu, F. Wu, Z. Yu, L. Zhu, J. Zhou, P. Yan, and W. Hong, "SIW cavity-fed filtennas for 5G millimeter-wave applications," *IEEE Transactions on Antennas and Propagation*, Vol. 69, No. 9, 5269–5277, 2021.

[8] Iqbal, A., J. J. Tiang, S. K. Wong, M. Alibakhshikenari, F. Falcone, and E. Limiti, "Miniaturization trends in substrate integrated waveguide (SIW) filters: A review," *IEEE Access*, Vol. 8, 223 287–223 305, 2020.

[9] Sun, X., J. Ma, Y. Feng, J. Shi, and Z. Xu, "Compact substrate integrated waveguide filtering antennas: A review," *IEEE Access*, Vol. 10, 91 906–91 922, 2022.

[10] Nitas, M., M.-T. Passia, and T. V. Yioultsis, "Fully planar slow-wave substrate integrated waveguide based on broadside-coupled complementary split ring resonators for mmWave and 5G components," *IET Microwaves, Antennas & Propagation*, Vol. 14, No. 10, 1096–1107, 2020.

[11] Christogeorgos, O., M.-T. Passia, M. Nitas, and T. V. Yioultsis, "Design of fully-planar CSRR-based substrate integrated waveguide circuits," in *2019 International Conference on Electromagnetics in Advanced Applications (ICEAA)*, 0289–0293, Granada, Spain, Sep. 2019.

[12] Nitas, M., V. Salonikios, S. Raptis, and T. V. Yioultsis, "Analysis and design of fully planar CSRR-enhanced substrate-integrated waveguides and slot antennas for 5G communications," in *2018 7th International Conference on Modern Circuits and Systems Technologies (MOCAST)*, 1–5, Thessaloniki, Greece, May 2018.

[13] Passia, M.-T. and T. V. Yioultsis, "A uniplanar substrate integrated waveguide based on edge-coupled complementary split-ring resonators for millimeter-wave components," in *2021 15th European Conference on Antennas and Propagation (EuCAP)*, 1–5, Dusseldorf, Germany, Mar. 2021.

[14] Amanatiadis, S. A., V. Salonikios, M. Nitas, T. Zygiridis, N. V. Kantartzis, and T. V. Yioultsis, "Sensitivity analysis of metamaterial-inspired SIW focusing on resonator misalignment," *IEEE Access*, Vol. 12, 63 942–63 949, 2024.

[15] Nitas, M., V. Salonikios, and T. V. Yioultsis, "Alternative finite element eigenvalue formulations for the simulation of arbitrarily bianisotropic media," *IEEE Transactions on Microwave Theory and Techniques*, Vol. 71, No. 2, 570–578, 2023.

[16] Nitas, M., C. S. Antonopoulos, and T. V. Yioultsis, "E-B eigenmode formulation for the analysis of lossy and evanescent modes in periodic structures and metamaterials," *IEEE Transactions on Magnetics*, Vol. 53, No. 6, 1–4, 2017.

[17] Nitas, M., V. Salonikios, S. Amanatiadis, and S. Arslanagic, "Field-flux finite element formulation for wave propagation in bianisotropic media," in *2023 17th European Conference on Antennas and Propagation (EuCAP)*, 1–4, Florence, Italy, Mar. 2023.

[18] Salonikios, V., M. Nitas, S. Raptis, and T. Yioultsis, "Computational analysis of graphene-based periodic structures via a three-dimensional field-flux eigenmode finite element formulation," *Progress In Electromagnetics Research M*, Vol. 92, 157–167, 2020.

[19] Nitas, M. and T. V. Yioultsis, "Electromagnetic parameter retrieval technique utilizing eigenvalue analysis and field averaging," *Journal of Applied Physics*, Vol. 131, No. 11, 2022.

[20] Nitas, M., M. Kafesaki, and S. Arslanagic, "Metasurface characterization based on eigenmode analysis and averaging of electromagnetic fields," *Journal of Applied Physics*, Vol. 134, No. 12, 2023.

[21] Nitas, M. and T. V. Yioultsis, "Characterization of edge-coupled broadside-coupled and complementary split-ring resonator periodic media based on numerical solutions of eigenvalue problems," *IEEE Transactions on Microwave Theory and Techniques*, Vol. 69, No. 12, 5259–5269, 2021.

[22] Lin, Y., Y. Zhang, H. Liu, Y. Zhang, E. Forsberg, and S. He, "A simple high-gain millimeter-wave leaky-wave slot antenna based on a bent corrugated SIW," *IEEE Access*, Vol. 8, 91 999–92 006, 2020.

[23] Singh, J., F. L. Lohar, and B. S. Sohi, "Design of dual band millimeter wave antenna using SIW material for 5G cellular network applications," *Materials Today: Proceedings*, Vol. 45, 5405–5409, 2021.

[24] Lyu, Y.-L., X.-X. Liu, P.-Y. Wang, D. Erni, Q. Wu, C. Wang, N.-Y. Kim, and F.-Y. Meng, "Leaky-wave antennas based on non-cutoff substrate integrated waveguide supporting beam scanning from backward to forward," *IEEE Transactions on Antennas and Propagation*, Vol. 64, No. 6, 2155–2164, 2016.

[25] Javanbakht, N., B. Syrett, R. E. Amaya, and J. Shaker, "A review of reconfigurable leaky-wave antennas," *IEEE Access*, Vol. 9, 94 224–94 238, 2021.

[26] Chen, Y., L. Zhang, Y. He, C. Mao, and S. S. Gao, "A low-cost, quad-beam, dual-polarized, 2-D leaky wave antenna with wide-angle beam scanning for millimeter-wave applications," *IEEE Transactions on Antennas and Propagation*, Vol. 71, No. 9, 7342–7353, 2023.

[27] Li, W.-H., B. Wu, H.-R. Zu, T. Su, and Y.-F. Fan, "Design of leaky-wave antenna with wide-angle backfire-to-forward beam scanning based on generalized pattern synthesis," *IEEE Transactions on Circuits and Systems II: Express Briefs*, Vol. 70, No. 7, 2625–2629, 2023.

[28] Arya, V., T. Garg, and H. M. R. Al-Khafaji, "SIW leaky wave antenna for THz applications," *Electronics*, Vol. 12, No. 8, 1839, 2023.

[29] Zheng, D., C. H. Chan, and K. Wu, "Leaky-wave structures and techniques for integrated front-end antenna systems," *IEEE Journal of Microwaves*, Vol. 3, No. 1, 368–397, 2022.

[30] Ali, M. Z. and Q. U. Khan, "High gain backward scanning substrate integrated waveguide leaky wave antenna," *IEEE Transactions on Antennas and Propagation*, Vol. 69, No. 1, 562–565, 2020.

[31] Esquius-Morote, M., B. Fuchs, J.-F. Zürcher, and J. R. Mosig, "A printed transition for matching improvement of SIW horn antennas," *IEEE Transactions on Antennas and Propagation*, Vol. 61, No. 4, 1923–1930, 2013.

[32] Chen, Y., L. Zhang, Y. He, C. Mao, S.-W. Wong, W. Li, P. Chu, and S. Gao, "Broadband high-gain SIW horn antenna loaded with tapered multistrip transition and dielectric slab for mm-Wave application," *IEEE Transactions on Antennas and Propagation*, Vol. 70, No. 7, 5947–5952, 2022.

[33] Zhang, Y., J.-Y. Deng, D. Sun, J.-Y. Yin, and L.-X. Guo, "Compact slow-wave SIW H-plane horn antenna with increased gain for vehicular millimeter wave communication," *IEEE Transactions on Vehicular Technology*, Vol. 70, No. 7, 7289–7293, 2021.

[34] Chen, Y., L. Zhang, Y. He, S.-W. Wong, W. Li, and S. Gao, "A broadband high-gain H-plane SIW horn antenna," in *2020 International Conference on Microwave and Millimeter Wave Technology (ICMMT)*, 1–3, Shanghai, China, Sep. 2020.

[35] Cao, Y., Y. Cai, L. Wang, Z. Qian, and L. Zhu, "A review of substrate integrated waveguide end-fire antennas," *IEEE Access*, Vol. 6, 66 243–66 253, 2018.

[36] Liu, L., T.-L. Bai, J.-Y. Deng, D. Sun, Y. Zhang, T. Yong, S.-G. Zhou, and L.-X. Guo, "Substrate integrated waveguide filtering horn antenna facilitated by embedded via-hole arrays," *IEEE Antennas and Wireless Propagation Letters*, Vol. 19, No. 7, 1187–1191, 2020.

[37] Haghparast, A. H. and P. Rezaei, "High performance H-plane horn antenna using groove gap waveguide technology," *AEU — International Journal of Electronics and Communications*, Vol. 163, 154620, 2023.

[38] Wang, J., F. Wu, Z. H. Jiang, Y. Li, and D. Jiang, "A millimeter-wave substrate integrated waveguide H-plane horn antenna with enhanced gain and efficiency," *IEEE Antennas and Wireless Propagation Letters*, Vol. 21, No. 4, 769–773, 2022.

[39] Huang, S., K. Y. Chan, and R. Ramer, "Dielectric-loaded SIW H-plane horn antenna with gradient air slots," *IEEE Antennas and Wireless Propagation Letters*, Vol. 20, No. 1, 43–47, 2020.

[40] Esfandiarpour, S. and A. Mallahzadeh, "Wideband H-plane horn antenna based on ridge substrate integrated waveguide," *IEEE Antennas and Wireless Propagation Letters*, 2012.

[41] Liu, L., T.-L. Bai, J.-Y. Deng, D. Sun, Y. Zhang, T. Yong, S.-G. Zhou, and L.-X. Guo, "Substrate integrated waveguide filtering horn antenna facilitated by embedded via-hole arrays," *IEEE Antennas and Wireless Propagation Letters*, Vol. 19, No. 7, 1187–1191, 2020.

[42] Wang, L., X. Yin, S. Li, H. Zhao, L. Liu, and M. Zhang, "Phase corrected substrate integrated waveguide H-plane horn antenna with embedded metal-via arrays," *IEEE Transactions on Antennas and Propagation*, Vol. 62, No. 4, 1854–1861, 2014.

[43] Wang, L., M. Esquius-Morote, H. Qi, X. Yin, and J. R. Mosig, "Phase corrected H-plane horn antenna in gap SIW technology," *IEEE Transactions on Antennas and Propagation*, Vol. 65, No. 1, 347–353, 2016.